Carbohydrate Polymers 347 (2025) 122730

Contents lists available at ScienceDirect

Carbohydrate Polymers

journal homepage: www.elsevier.com/locate/carbpol

Associating structural characteristics to immunomodulating properties of carrot rhamnogalacturonan-I fractions

Krishna Desai [a,b,c], Justyna M. Dobruchowska [a], Kari Elbers [b], Justyna Cybulska [d], Artur Zdunek [d], Mojtaba Porbahaie [e], Erik Jansen [e], Joost Van Neerven [e], Ruud Albers [c], Tom Wennekes [a], Annick Mercenier [c], Henk A. Schols [b,*]

[a] Department of Chemical Biology and Drug Discovery, Utrecht Institute for Pharmaceutical Sciences and Bijvoet Center for Biomedical Research, Utrecht University, Universiteitsweg 99, 3584 CG Utrecht, the Netherlands
[b] Laboratory of Food Chemistry, Wageningen University, Bornse Weilanden 9, 6708 WG Wageningen, the Netherlands
[c] NutriLeads B.V., Bronland 12N, 6708 WH Wageningen, the Netherlands
[d] Institute of Agrophysics, Polish Academy of Sciences, Ul Doświadczalna 4, 20-290 Lublin, Poland
[e] Cell Biology and Immunology, Wageningen University & Research, De Elst 1, 6700 HB Wageningen, the Netherlands

ARTICLE INFO

Keywords:
Rhamnogalacturonan
Size fractionation
Structural characterization
Acetylated pectic polysaccharides
Saponification
Structure-function activity
Immunomodulation

ABSTRACT

Carrot rhamnogalacturonan-I (cRG-I) is a polydisperse polysaccharide with molecular weights of 7–250 kDa. Using size exclusion chromatography cRG-I was fractionated and pooled in fractions (PF1–6). All fractions contained the same RG-I monosaccharides and similar glycosidic linkages although in varying relative amounts. The main differences were in rhamnose substitution, arabinan- and galactan side chain length and in levels of acetylation and methyl esterification. Atomic force microscopy showed either spheric or elongated structures for cRG-I and its derived fractions. To gain insight in the structure-function relationship of cRG-I, the immunomodulatory effect of the six fractions and their saponified derivatives was assessed in vitro. All fractions, except PF2, dose-dependently stimulated TNFα, IL-6, IL-1β, IL-8 and IL-10 production in peripheral blood mononuclear cells (PBMCs) of three healthy donors. Cytokine levels were largely influenced by the Mw and degree of esterification of the individual fractions. Notably, the highest Mw fraction (100 kDa) displayed the most potent activity, which was strongly reduced after the removal of ester residues by saponification. In contrast, the 75 kDa Mw population (PF2) proved inactive while its saponified counterpart exhibited substantial immunomodulatory activity. This confirmed the role of ester residues on the immune profile of RG-I subpopulations.

1. Introduction

Dietary fibres play a key role in sustaining a healthy life (Reynolds et al., 2019). The beneficial health effect of different dietary fibres has been intensely investigated over the past decades. Among them, pectin polysaccharides have received increasing attention (Beukema et al., 2020; Roman-Benn et al., 2023). Pectin is a major constituent of dicotyledonous plant cell walls. Pectin is a large and polydisperse polysaccharide comprising three pectic structural elements i.e. homogalacturonan (HG), rhamnogalacturonan-I (RG-I) and substituted homogalacturonans like rhamnogalacturonan-II (RG-II) and xylogalacturonan (Voragen et al., 2009). HG, also known as the "smooth region" of pectin, is the most prominent structural element in pectin and typically makes up to 65 % of total pectin in a plant. HG is a

Abbreviations: AFM, atomic force microscopy; AG, arabinogalactan; Ara, arabinose; AUC, area under the curve; cRG-I, carrot derived rhamnogalacturonan-I; DA, degree of acetylation; Dha, 3-deoxy-D-lyxo-2-heptulopyranosylaric acid; DMSO, dimethyl sulfoxide; Fuc, fucose; Gal, galactose; GalA, galacturonic acid; GC, gas chromatography; Glc, glucose; GlcA, glucuronic acid; HCl, hydrochloric acid; HG, homogalacturonan; HPAEC-PAD, High-Performance Anion-Exchange Chromatography with Pulsed Amperometric Detection; HPLC, high-performance liquid chromatography; HPSEC, high-performance size exclusion chromatography; HS, head space; HSQC, heteronuclear single quantum coherence; KDa, kilodalton; Kdo, 2-keto-3-deoxy-manno-octulosonic acid; LPS, lipopolysaccharide; Man, mannose; mhdp, metahydroxydiphenyl; MS, mass spectrometry; Mw, average molecular weight; NaOH, sodium hydroxide; NMR, nuclear magnetic resonance; PBMC(s), peripheral blood mononuclear cells; PF, pooled fractions; PMAA, partially methylated alditol acetate; RG-I, rhamnogalacturonan-I; RG-II, rhamnogalacturonan-II; Rha, rhamnose; SCFA, short-chain fatty acids; SEC, size exclusion chromatography; TFA, trifluoracetic acid; Xyl, xylose.

* Corresponding author.
E-mail addresses: k.v.desai@uu.nl, krishna.desai@wur.nl (K. Desai), henk.schols@wur.nl (H.A. Schols).

https://doi.org/10.1016/j.carbpol.2024.122730
Received 7 July 2024; Received in revised form 20 August 2024; Accepted 6 September 2024
Available online 10 September 2024

homopolymer consisting of 1, 4-linked α-D-GalA residues that can be methyl-esterified at C-6 or, less commonly, acetylated at *O*-2 and/or *O*-3. The substitution of HG by single or oligomeric D-xylose results in xylogalacturonan. Another substituted HG segment, RG-II, contains 11 different monosaccharides including rare sugars like apiose, aceric acid, 2-keto-3-deoxy-manno-octulosonic acid (Kdo) and 3-deoxy-D-lyxo-2-heptulopyranosylaric acid (Dha) that create complex but conserved side chains attached to a backbone of around eight GalA-residues. The most diverse pectin structural element is RG-I that has a distinct backbone consisting of galacturonic acid (GalA) and rhamnose (Rha) diglycosyl repeating units [→2)-α-L-Rha*p*-(1 → 4)-α-D-Gal*p*A-(1→]. The backbone may be acetylated at the *O*-2 and/or *O*-3 position of GalA residue and may carry neutral sugar side chains like arabinan, galactan and arabinogalactan (AG) type I or type II at the *O*-3 and/or *O*-4 position of Rha residue (Voragen et al., 2009; Yapo, 2011). Arabinan is commonly a linear chain of α-(1, 5)-linked-L-Ara*f* that can be branched at *O*-2 and *O*-3 position by α-L-Ara*f*-(1 → 2) and/or α-L-Ara*f*-(1 → 3) (Yapo, 2011). Galactan is composed of β-(1, 4)-linked-D-Gal*p* that may carry β-(1, 6)-linked-D-Gal*p* (Caffall & Mohnen, 2009). AG-I has the same β-(1, 6)-linked galactan backbone, but comprises one or more α-L-Ara*f* residues. AG-II is a branched polymer associated with the AG protein and is composed of a β-1,3 galactan backbone with β-1,6-Gal side chain(s) and terminal Ara residues at the *O*-3 and *O*-6 positions (Voragen et al., 2009; Yapo, 2011).

Precise pectin structures strongly depend on the plant source, tissue, and developmental stage and this diversity may lead to different biological functions within the plants, but after ingestion, also in mammals (Voragen et al., 2009; Yapo, 2011). The most commonly studied pectin sources include citrus peel, sugar beet and apple due to their industrial application for gel-forming and thickening properties (Dranca & Oroian, 2018). Some of these commercial pectins have also been reported to exert various effects on the human body, e.g. by direct interaction with host immune cells and by modulation of the gut microbiota and the production of SCFA (Beukema et al., 2020). Pectin's beneficial effect on chronic diseases has mostly been studied in animal models (Donadio & Fabi, 2024) but also in human intervention studies (Brouns et al., 2012; Schwab et al., 2006). The commercial pectin extracts however are relatively poor in RG-I content due to their production process focusing on enrichment of the HG domain (Voragen et al., 2009).

RG-I domains constitute 20–40 % of pectin in common crops and are naturally embedded in the plant cell wall matrix (Voragen et al., 2009; Yapo, 2011). In contrast to the widely studied and structurally simple HG (Jermendi et al., 2023), RG-I and RG-II have significantly more complex structures that remain very challenging to elucidate (Barnes et al., 2021). The RG-II domain is a minor constituent of pectin and is well conserved throughout the plant kingdom (Voragen et al., 2009). Wine-derived RG-II structure and its degradation by gut bacteria has been studied in detail (Barnes et al., 2021; Ndeh et al., 2017). However, RG-II populations have often been ignored within extracted pectin material. In contrast to RG-II, the structure of RG-I strongly depends on the source material and isolation process. Numerous structural studies have been performed on a large variety of RG-I extracts of variable purity, originating from different sources and extracted using different chemical or enzymatic extraction methods (Niu et al., 2023). RG-I and RG-II containing extracts from different sources have been studied in various in vitro biological assays, establishing their immunomodulating capacity (Ho et al., 2016; Kiyohara et al., 2002; Lee et al., 2021; Son et al., 2023). In the last few decades, experimental models of animal diseases have demonstrated protective effects of pectic polysaccharides against e.g. intestinal inflammation and metabolic dysfunction (Huang et al., 2017; Kwak et al., 2019; Niu et al., 2023; Tang & de Vos, 2023).

Notably, unlike HG, the reproducible production of highly enriched RG-I extracts at the industrial scale is challenging thus limiting their application in clinical studies. The standardized production of RG-I extracted from carrot pomace (cRG-I) at an industrial scale has recently been reported (McKay et al., 2021) and this extract was used to study biological functions. Fecal fermentation experiments highlighted that cRG-I beneficially modulates the gut microbiota leading to an increased production of short chain fatty acids (SCFA) (Van den Abbeele et al., 2020; Van den Abbeele et al., 2021). cRG-I was also shown to activate immune cells in vitro for example by stimulating the production of cytokines by peripheral blood mononuclear cells (PBMCs) (McKay et al., 2021). Importantly, cRG-I has recently been demonstrated to reduce the duration and severity of common cold symptoms in a rhinovirus challenge trial conducted in healthy adults (Lutter et al., 2021; McKay et al., 2022). In this randomized, double-blind, placebo-controlled study, dietary supplementation of cRG-I accelerated the protective local immune responses to a standardized respiratory infection. Daily intake of cRG-I also enhanced natural killer cell responses ex vivo (McKay et al., 2022). However, the structural complexity of cRG-I has so far limited the possibility of addressing structure-function related questions and the role of its structural elements in immune modulation.

In this work, we aimed to gain a better insight into the structure activity relation for the immunomodulatory effects of cRG-I. Fractions obtained using medium scale size-fractionation of cRG-I were characterized using linkage analysis, NMR and AFM imaging. To assess the structure-function relationship, the immunomodulating activity of six fractions and their saponified, i.e. de-esterified, counterparts were assessed in an in vitro PBMC assay.

2. Material and methods

2.1. Material

cRG-I was provided by NutriLeads BV (Wageningen, The Netherlands). cRG-I was extracted at industrial scale from carrot pomace using common food processing methods (McKay et al., 2021) including aqueous extraction at 45 °C in the presence of Pectinex™ Ultra Mash (Novozymes, Bagsværd, Denmark), decanting and filtration to remove non-soluble residues, filtration to remove small molecules, pasteurization and subsequent spray-drying of the RG-I enriched polysaccharide extract.

2.2. Fractionation of cRG-I by size exclusion chromatography

The medium-scale preparative size exclusion (SEC) chromatography was performed using the AKTA pure 150 M explorer system (GE Healthcare, Boston, Boston, UK) equipped with a Superdex 200 PG column (10 × 53 cm; GE Healthcare) and a Shodex RI-101 refractive index detector (Showa Denko K·K, Tokyo, Japan). Briefly, 2 g cRG-I was loaded on the column and eluted with 20 mL/min of 0.1 M ammonium acetate buffer (pH 5.5). Two successive runs resulted in 25 large fractions (140 mL) that were further characterized using High-Performance Size Exclusion Chromatography (HPSEC) to determine their hydrodynamic volume, and automated colorimetry metahydroxydiphenyl (mhdp) and orcinol-sulphuric acid assays (autoanalyzer, Skalar Analytical BV, Breda, The Netherlands) to measure uronic acids and neural sugars, respectively (Blumenkrantz & Asboe-Hansen, 1973; Thibault, 1979). Based on HPSEC and colorimetric assays, fractions were pooled into six distinct populations as indicated in Fig. 1A. Pools were desalted using multiple rounds of freeze-drying and named PF1, PF2, PF3, PF4, PF5 and PF6 from high to low Mw.

2.3. High-performance size exclusion chromatography (HPSEC)

The molecular weight distribution of cRG-I and cRG-I fractions was analysed using HPSEC on an Ultimate 3000 HPLC (Dionex, Sunnyvale, CA, USA) equipped with a Shodex RI-101 refractive index detector (Showa Denko K.K.) as described previously (Desai et al., 2024). Columns were calibrated with pullulans (Polymer Laboratories, Palo Alto, CA, USA) and covered a molecular weight range of 0.2 to 880 kDa for pullulans. The data were analysed using Chromeleon 7.3 software

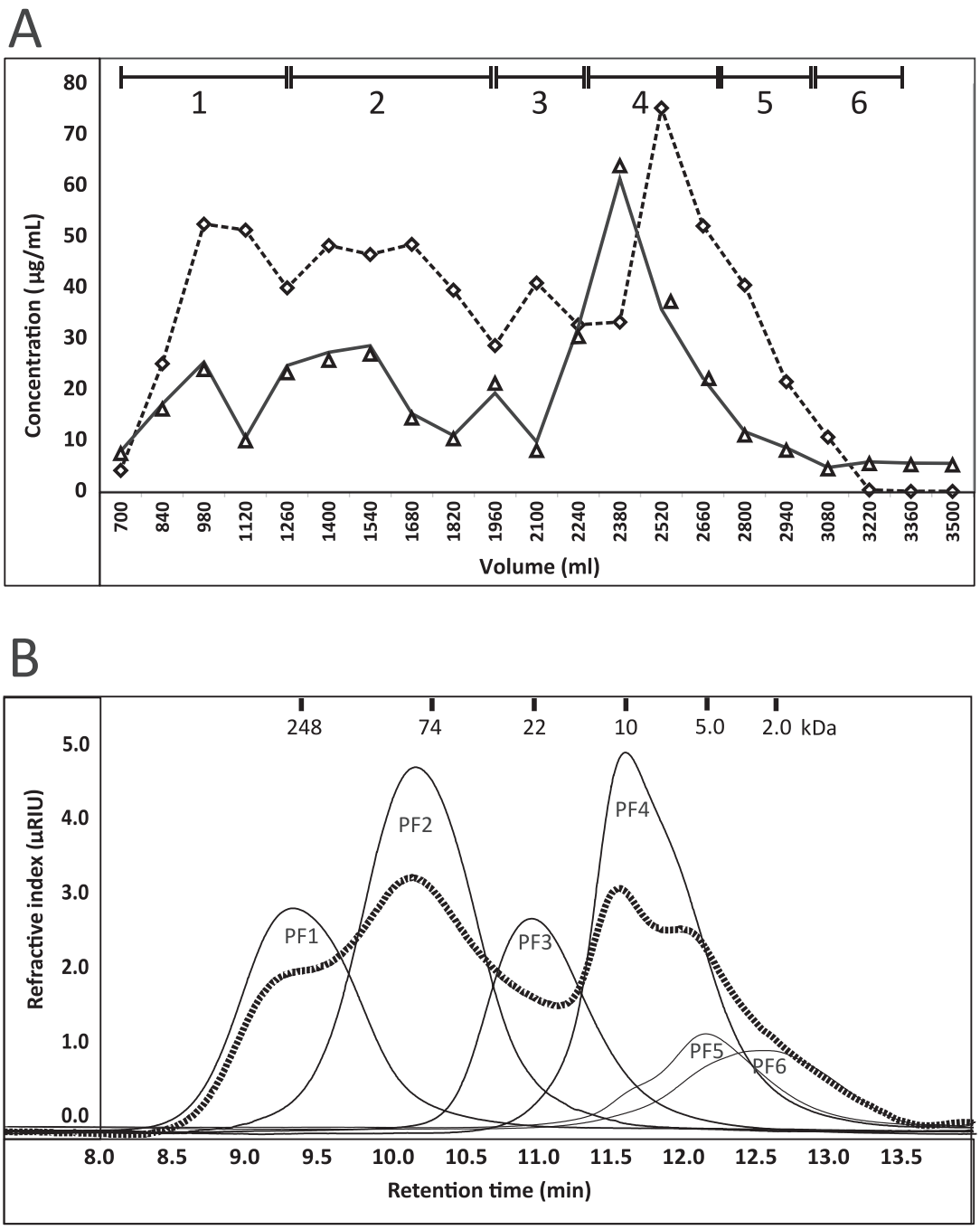

Fig. 1. A) Size exclusion chromatography on Superdex 200 PG of cRG-I: ■ ■ ■ ■ ■, neutral sugars; ▬▬▬, uronic acids. The pooled fractions PF1–6 are indicated B) High performance size exclusion chromatography elution pattern of cRG-I (dotted line) and its fractions PF1-6. The molecular weights of pullulan standards are labelled at the corresponding retention time.

(Dionex).

2.4. Sugar composition analysis

Methanolysis and High-Performance Anion Exchange Chromatography (HPAEC) analysis were conducted with a minor modification of the previously published method (De Ruiter et al., 1992). cRG-I and fractions thereof were methanolized in 3 M methanolic HCl at 80 °C for 16 h, dried under N_2 followed by TFA hydrolysis at 121 °C for 2 h. The released monosaccharides were analysed by HPAEC equipped with a pulsed Amperometric detector (HPAEC-PAD) using an ICS-5000 HPLC (Dionex) system equipped with a CarboPac PA1 guard column (2 mm ID × 50 mm) and CarboPac PA1 column (2 mm × 250 mm) (Dionex) as previously described (Desai et al., 2024). Monosaccharide standards (1–25 µg/mL) were included in the analysis for quantification. The analyses were conducted in duplicate, and results are expressed in anhydrous sugars as mean values ± standard deviation.

2.5. Linkage analysis

The glycosidic linkage analysis was done as described before (Black et al., 2021). Briefly, the samples with non-reduced or reduced uronic acid were dissolved in DMSO and three times permethylated. The permethylated samples were hydrolysed using 2 M TFA for 120 min at 121

°C. The hydrolysates were reduced with $NaBD_4$ and acetylated. The resulting partially methylated alditol acetates were analysed using GC (TRACE GC ultra, Thermo Scientific, Waltham, MA, USA) interfaced with a dual stage quadrupole mass selective detector (DSQII, Thermo Scientific) and separation was performed using a 60 m Rxi®-5MS column (Restek, Bellefonte, PA, USA) with 0.25 mm diameter and 0.25 μm film thickness. One μL sample was injected in the PTV split mode with the injector operating at initial temperature of 190 °C ramped to 275 °C at 14.5 °C/min, hold for 1.0 min. The GC oven was set at an initial temperature of 120 °C raised to 250 °C at 2.5 °C/min with hold for 5 min. Mass range: 50–450 *m/z*. The collected data were analysed using Xcalibur™ software (Thermo Scientific) and chromatogram peaks were identified using an inhouse database.

2.6. NMR spectroscopy

1D and 2D NMR spectra were recorded on a 600 MHz Bruker Avance NEO NMR spectrometer equipped with a 5 mm TCI Prodigy CryoProbe (Bruker Corporation, Billerica, MA, USA). Samples were dissolved in D_2O (0.6 mL 99.9 %; Cambridge Isotope Laboratories, Tewksbury, MA, USA) and transferred to 5 mm NMR tubes. ^1H and ^{13}C NMR spectra were obtained using Bruker pulse programs. Multiplicity-edited ^1H—^{13}C HSQC were recorded with 1536 data points in F2 and 256 in F1. ^1H chemical shifts were referenced to internal sodium 3-trimethylsilyl-(2,2,3,3-$^2H_4$)-propanoate (TSP, δ_H 0.00). Data were processed by using MestReNova software (Mestrelab Research S.L., Santiago de Compostela, Spain).

2.7. Oligosaccharide analysis using MALDI-TOF MS

One μL of the premix containing 0.5 μL sample (1.0 mg/mL) and 0.5 μL of DHB matrix solution (10 mg/mL DHB in H_2O) was spotted on a Matrix-Assisted Laser Desorption Ionization (MALDI) plate (Bruker Corporation) that was dried under a warm air stream resulting in crystal formation. Samples were further analysed using Bruker-Autoflex Max MALDI Time-Of-Flight Mass spectrometry (TOF MS) (Bruker Daltonics) as described previously (Desai et al., 2024). The data was analysed using the flexAnalysis 3.3 software (Bruker Corporation).

2.8. Atomic force microscopy imaging

AFM height images were obtained using Multimode 8 with a Nanoscope V controller (Bruker Corporation) using the semiautomatic high-speed tapping mode. A silicon nitride cantilever with a 2 nm-nominal radius pyramidal tip, a nominal resonance frequency of 130 kHz and a nominal spring constant of 0.4 N/m (ScanAsyst Air, Bruker Corporation) was applied. The following scan settings were established: scan size 2 × 2 μm and 5 × 5 μm, resolution 512 × 512 points and scan rate 2.0 Hz. Twenty μL of the 0.1 mg/mL of cRG-I or individual pooled fractions (PF1–6) solution (pH 7) was dropped onto freshly cleaved mica and spread by a spin coater SPIN150i (SPS-EUROPE, Putten, The Netherlands). Next, the sample was dried in a desiccator (relative humidity RH = 15 %) at 22 °C overnight before the AFM studies. These studies were executed in ambient air at room temperature and RH = 25–30 %. At least ten images were collected for each sample.

AFM height images were processed and analysed using SPIP 6.2.0 software (Image Metrology, Hørsholm, Denmark). Prior to analysis, all images were flattened using a third order polynomial fitting and global bow removal, filtered using a standardized roughness filter and noise reduction procedure, and smoothed by Gaussian filtering. The geometrical parameters of macromolecules were determined using the 'Particle & Pore Analysis' module of SPIP software (Cybulska et al., 2016). A set of pixel thresholds which included cutting out elements lower than 20 pm in the Z direction and the segmentation of particles if the minima between them were below 10 pm was applied for all AFM images. Area, elongation and median height parameters were used for object characterization. Definitions of parameters are described in the SPIP Reference Guide (SPIP Reference guide, 2024).

The results obtained from AFM image analysis were treated by one-way Anova and post hoc (HSD) Tukey's test at 0.05 significance level (Statistica software v. 13, StatSoft, Cracow, Poland). Statistically significantly different results ($p < 0.05$) were designated by different letters.

2.9. Degree of esterification

Samples were treated with 0.1 M NaOH for 1 h at 4 °C followed by 23 h at RT to release the methyl esters and acetyl groups. The released methanol was quantified using headspace gas chromatography (HS GC) according to Huisman et al. (2004). The collected data were analysed using Xcalibur 4.1 software (Thermo Scientific). The samples after HS GC analysis were cooled at 4 °C for 1 h and then centrifuged (16.000 *g*, 10 min) to analyse the acetyl content. The released acetic acid was measured by HPLC ultimate 3000 system (Dionex) as described before (Desai et al., 2024). Data were analysed using Chromeleon 7.2 software (Dionex). The degree of methyl esterification (DM) and acetylation (DA) are expressed as the percentage of the total number of GalA residues methoxylated or acetylated, respectively.

2.10. Removal of esters: saponification

The methyl ester and acetyl groups of cRG-I or fractions thereof (5 mg/mL) were hydrolysed with 0.1 M NaOH for 24 h at 4 °C, neutralized and filtered using a pyrogen-free 3 kDa cutoff centrifuge tube (Merck KGaA, Darmstadt, Germany) and the retentate was freeze dried.

2.11. Pectin structure indicators

Total RG-I and HG content present in cRG-I extract and PF fractions were calculated using the Eqs. (1) & (2):

$$Total\ RG-I\ mol\% = \{Ara + Gal + (2{*}Rha)\} \quad (1)$$

$$HG\ backbone\ mol\% = \{GalA–Rha\} \quad (2)$$

The DM and DA were calculated based on an assumption that all methyl and acetyl groups are present on GalA using the Eqs. (3) & (4):

$$DM\% = \frac{Released\ methanol–free\ methanol}{GalA}{*}100 \quad (3)$$

$$DA\% = \frac{Released\ acetic\ acid–free\ acetic\ acid}{GalA}{*}100 \quad (4)$$

2.12. Peripheral Blood Mononuclear Cells (PBMC) assay

PBMCs were isolated from three buffy coats obtained from healthy donors (Sanquin blood bank, Nijmegen, The Netherlands) using gradient centrifugation on Ficoll Paque Plus (GE Healthcare, Chicago, IL, USA), following standard procedures (Porbahaie et al., 2024). The isolated PBMCs were cryopreserved in liquid nitrogen until the day of the experiment. On the experiment day, PBMCs were thawed, and the concentration was adjusted to 2×10^6 cells/mL. Subsequently, 100 μL of the cells were added to each well of a 96-well culture plate (Corning, Glendale, AZ, USA), resulting in a density of 2×10^5 cells per well. The plate was then incubated at 37 °C for one hour. Following incubation, test samples, LPS (1 μg/mL) and RPMI medium as the positive and negative controls, respectively - were added to the wells. The plates were further incubated for 20 h at 37 °C with 5 % CO_2. After incubation, 20 μL of the culture supernatant was collected in a 96-well NUNC plate (Fisher Scientific, Hampton, NH, USA) and diluted 10 times using RPMI medium. The diluted culture supernatant was frozen at −20 °C until cytokine measurement. Cytokine levels, including IL-1β, IL-6, IL-8, IL-

10, IL-12p70 and TNF-α in the culture supernatant were quantified using the Human Inflammatory Cytokine kit (BD biosciences, Franklin Lakes, NJ, USA) following the manufacturer's protocol. IL-12 values were below the detection limit and thus not considered. Data analysis was performed using FCAP Array Software v3.0 (BD Biosciences). PBMC data were normalized to the LPS-induced cytokine values for each donor and each cytokine, where data for positive control (LPS) were set at 1. Graphical representation was done with GraphPad Prism v10.0 software (San Diego, CA, USA).

3. Results and discussion

3.1. Structural features of cRG-I

cRG-I was isolated from carrot pomace, a side stream of carrot juice production. The water-soluble cRG-I extract composition has been described previously (Desai et al., 2024; McKay et al., 2021) (Supplementary Table 1). cRG-I was rich in carbohydrates (78–82 % *w*/w), mainly composed of GalA (27 mol%), Rha (17 mol%), Ara (29 mol%), and Gal (18 mol%) residues that together correspond to approximatively 90 w/w% of the carbohydrate monomers. The 10 % remaining saccharides were Fuc, Glc and GlcA. The GalA:Rha ratio (≈ 1.4) indicates that the extract contains predominantly RG-I with some stretches of HG. The degree of acetylation (DA) was high (60 %) and degree of methyl esterification (DM) was low (12 %). The side chains (47 mol%) were largely composed of Ara and Gal with a Gal:Ara ratio equal to 0.6, suggesting a higher abundance of arabinan than (arabino)galactan domains. The HPSEC profile of cRG-I revealed the polydispersity of the extract with Mw populations between 7 and 250 kDa based on pullulan standards (see Fig. 1B).

3.2. Fractionation of cRG-I using preparatory size exclusion chromatography

The homogeneity and Mw of cRG-I was determined using HPSEC that showed distinct populations that were separated by size-fractionation (Fig. 1B). The SEC fractions containing carbohydrates were next pooled in 6 composite fractions based on HPSEC and colorimetry assays (Fig. 1A). These pooled fractions (PFs) were named PF1–6. Almost all soluble cRG-I material (99 %) was retrieved in the six pooled fractions with a yield of 18 %, 29 %, 11 %, 24 %, 9 % and 8 % for PF1–6, respectively. HPSEC analysis showed that they all had a rather distinct Mw distribution (Fig. 1B). PF1–6 were narrowly dispersed, well separated according to their hydrodynamic volume, and showed decreasing apparent Mw on HPSEC-RI: PF1 = 248 kDa, PF2 = 74 kDa, PF3 = 22 kDa, PF4 = 10 kDa, PF5 = 5 kDa and PF6 = 3.5 kDa.

3.3. Monosaccharide composition of cRG-I Mw populations

The monosaccharide analysis showed that the cRG-I starting extract (supplementary Table 1) and its derived fractions are all composed mainly of the four characteristic RG-I sugars Ara, Rha, Gal and GalA which concurred with previously determined RG-I overall composition by us and others (Desai et al., 2024; McKay et al., 2021). However, the amounts of these monosaccharide moieties varied per Mw fraction (Table 1). Ara was the dominant sugar residue in all fractions with steadily increasing levels from the high Mw fractions PF1 and PF2 (≈ 29 mol%) to the low Mw fraction PF6 (65 mol%). The Gal content of the fractions showed an opposite trend with nearly 27 mol% for the high Mw fractions PF1 and PF2, progressively decreasing for the lower Mw fractions down to almost 7 mol% in PF5 and PF6. The amount of Rha was similar (≈ 20 mol%) for PF1 to PF4 but was clearly lower in the PF5 and PF6 fractions (≈ 13 and ≈ 7 mol%, respectively). GalA was around 21–22 mol% in PF1 and PF2 and slightly higher in PF3 and PF5 (≈ 25 mol%). Compared to the other fractions, PF4 exhibited the highest level of GalA (≈ 31 mol%) while PF6 had the lowest GalA level (≈ 13 mol%). The other monosaccharides were present in relatively low amounts in all fractions except for Glc in PF5 and PF6 (≈ 3 mol%) and GlcA in PF4 (≈ 3 mol%).

The fractions PF1, PF2 and PF3 mainly contained highly acetylated RG-I (DA 72–98 %) with a low degree of methyl esterification (DM 7–9 %), and very little or no HG (≤ 3.5 %). In comparison to the higher Mw fractions, the fractions PF4, PF5 and PF6 were lower in RG-I content (80–87 %) and contained somewhat higher amounts of HG (5–13 %), reflecting stretches of the HG pectin backbone remaining after enzymatic treatment. Further, these fractions contained a lower degree of acetylation (DA 30–55 %) and a higher degree of methyl esterification (DM 23–40 %). The DM value that is relative to GalA translated to highly methylated HG in all fractions except PF2 where almost no HG was present pointing to some methylated RG-I backbone. The GalA/Rha ratio was close to 1.0 for PF1–3 and between 1.6 and 2.0 for PF4–6, in line with their individual RG-I and HG content. The Ara/Rha ratio, indicative of arabinan side chains linked to Rha residues, was similar for PF1–3 (1.4–1.5), slightly higher in PF4 (1.8) but notably higher in PF5 (3.8) and even more in PF6 (8.9). The Gal/Rha ratio was slightly higher in PF1 and PF2 (1.3–1.4) than in PF3 (1.0) and PF6 (0.9), and the lowest

Table 1
Monosaccharide composition (mol %), degree of esterification and structural characteristics of cRG-I fractions PF1–6. The yield % is defined as the recovered amount of pooled fraction over the amount of cRG-I loaded on the column for fractionation.

	PF1			PF2			PF3			PF4			PF5			PF6		
Yield % (w/w)	18.0			29.0			11.0			24.0			8.7			8.5		
Monosaccharides (mol%)																		
Ara	28.6	±	0.1	29.2	±	0.2	32.4	±	0.3	34.2	±	0.2	47.8	±	0.3	65.3	±	4.5
Rha	19.1	±	0.1	20.8	±	1.8	21.1	±	0.5	19.0	±	0.1	12.7	±	0.1	7.3	±	0.8
Gal	26.7	±	0.4	27.3	±	3.5	20.3	±	0.8	10.3	±	0.2	6.6	±	0.4	6.8	±	0.6
Fuc	0.5	±	0.0	0.3	±	0.1	0.4	±	0.0	1.6	±	0.1	1.1	±	0.2	0.4	±	0.0
Glc	0.5	±	0.2	0.0	±	0.0	0.4	±	0.1	0.8	±	0.3	2.6	±	0.3	3.4	±	0.2
Xyl	1.0	±	0.2	0.4	±	0.1	0.3	±	0.1	0.5	±	0.1	0.5	±	0.7	0.6	±	0.1
Man	0.0	±	0.0	0.0	±	0.0	0.0	±	0.0	0.0	±	0.0	1.2	±	0.0	1.5	±	0.1
GalA	22.3	±	0.1	21.2	±	1.4	24.6	±	1.3	30.6	±	0.2	25.5	±	0.6	12.8	±	4.2
GlcA	1.3	±	0.0	0.8	±	0.0	0.4	±	0.1	2.9	±	0.1	1.5	±	0.1	1.0	±	0.6
Total w/w%	86.0	±	2.7	86.6	±	3.2	85.6	±	6.5	79.9	±	1.6	69.6	±	1.3	69.4	±	5.9
DA%	97.7			94.6			71.7			29.8			33.9			55.2		
DM%	6.6			7.2			9.3			23.0			29.2			40.3		
RG-I%	93.6			98.1			95.0			82.5			79.8			86.8		
HG%	3.2			0.4			3.5			11.6			12.8			5.5		
GalA/Rha	1.2			1.0			1.2			1.6			2.0			1.7		
Ara/Rha	1.5			1.4			1.5			1.8			3.8			8.9		
Gal/Rha	1.4			1.3			1.0			0.5			0.5			0.9		

in PF4 and PF5 (0.5), suggesting rather short galactan side chains that differ between the fractions. Altogether these results point to the fact that cRG-I is composed of domains that differ in their detailed structure. Of note, combining the weighted averages of the different PF fractions added up to the values characterizing the composition of the parent cRG-I extract where total carbohydrate content averaged to 78 *w*/w% with Ara, Gal, Rha and GalA averaging to 29 mol%, 18 mol%, 17 mol% and 27 mol%, respectively, along with 61 % DA and 13 % DM (Supplementary Table 1).

However, monosaccharide composition analysis alone does not establish how many Rha residues are carrying side chains and if side chains along the RG-I backbone vary in length and composition. We therefore further investigated the structure by conducting linkage analysis and using 1D and 2D NMR.

3.4. Glycosidic linkages analysis of cRG-I fractions

The glycosidic linkage composition of cRG-I and its fractions is shown in Table 2. Parental cRG-I was derivatised with and without prior reduction to include acidic sugars in the analysis, which confirmed the presence of only terminal GalA and 1,4-linked GalA residues. The PF1–6 fractions were derivatised without prior reduction resulting in only PMAA of neutral sugars.

Table 2
Neutral sugar-linkage composition (mol%) of cRG-I and its fractions PF1–6, deduced from GC–MS analysis of per-*O*-methylated alditol acetates. Values in bold are total sugar deduced from GC–MS analysis and values in brackets are deduced from the methanolysis results for the neutral sugar composition. tr = traces.

Glycosidic linkage	cRG-I	PF1	PF2	PF3	PF4	PF5	PF6
T-Ara*f*	18.8	16.1	14.4	13.1	18.1	27.2	28.1
2-Ara*f*	0.5	0.3	0.3	0.4	0.3	0.3	0.4
3-Ara*f*	0.4	0.3	0.4	0.4	0.6	0.4	0.5
5-Ara*f*	18.6	13.6	14.8	17.7	21.6	29.2	37.6
3,5-Ara*f*	6.4	4.5	4.7	6.8	8	8.2	9.2
2,3,5-Ara*f*	4.5	4	3.7	5.3	4.4	3.6	3
Total Ara*f*	**49.2** (45.8)	**38.8** (36.5)	**38.1** (35.9)	**43.8** (41.7)	**53.1** (51.2)	**68.9** (67.7)	**78.9** (78.1)
T-Rha*p*	2.2	2.2	1.7	0.9	4	3.4	1.9
2-Rha*p*	6	4.3	5.1	11	9.3	4.7	2.9
4-Rha*p*	1.7	0.8	1.3	1.7	5.9	2.4	1.2
2,4-Rha*p*	11.8	14.7	13.9	11.5	6.7	3.7	2.2
3,4-Rha*p*	0.2	–	–	–	–	0.8	0.2
2,3,4-Rha*p*	–	–	–	–	–	0.3	–
Total Rha*p*	**21.8** (23.3)	**21.9** (24.4)	**22** (25.6)	**25.2** (27.2)	**25.8** (28.4)	**15.2** (18)	**8.4** (8.7)
T-Gal*p*	8.6	15.6	14.8	9.5	5.8	1	1.5
3-Gal*p*	1	0.9	1.1	1.4	0.5	0.4	0.3
4-Gal*p*	11.4	11.4	10.2	11.1	5.1	3.9	3.1
6-Gal*p*	1.2	3.4	3.5	1.8	1.1	0.9	0.9
2,4-Gal*p*	0.2	–	0.2	0.2	0.5	0.4	0.3
3,4-Gal*p*	0.2	0.2	0.3	0.2	–	0.2	0.2
2,6-Gal*p*	–	–	–	–	–	0.2	–
3,6-Gal*p*	0.6	0.7	1.4	0.3	–	0.3	0.1
4,6-Gal*p*	tr	–	–	–	–	–	–
3,4,6-Gal*p*	0.1	–	0.3	–	–	–	0.1
Total Gal*p*	**23.2** (25.9)	**32.3** (34.1)	**31.8** (33.6)	**24.5** (26.1)	**13** (15.4)	**7.3** (9.3)	**6.5** (8.1)
T-Fuc*p*	0.2	0.4	0.3	0.2	0.4	0.4	0.2
3-Fuc*p*	0.2	–	–	0.3	–	0.1	0.2
Total Fuc*p*	**0.4**	**0.4**	**0.3**	**0.5**	**0.4**	**0.5**	**0.4**
4-Glc*p*	1.2	0.6	–	tr	0.8	1.2	0.8
Total Glc*p*	**1.2**	**0.6**	**–**	**tr**	**0.8**	**1.2**	**0.8**
3-Api*f*	0.1	–	–	–	0.2	0.5	0.5
Total Api*f*	**0.1**	**–**	**–**	**–**	**0.2**	**0.5**	**0.5**

Linkage analysis confirmed the presence of arabinan, galactan, AG-I and AG-II side chains in cRG-I and the PF1–6 fractions, albeit in different proportions. The main Ara linkages were T-Ara*f*, 5-Ara*f*, 3,5-Ara*f*, and 2,3,5-Ara*f* with some 2-Ara*f* and 3-Ara*f* in all fractions indicating the prevalent occurrence of linear, single- and double-branched Ara moieties. Gal was mainly present as T-Gal*p* and 4-Gal*p,* next to 3-Gal*p,* 6-Gal*p*, 3,6-Gal*p* and occasionally some 2,4-Gal*p*, 3,4-Gal*p,* and 3,4,6-Gal*p* suggesting a higher prevalence of galactan over AG-II and AG-I structures. The presence of 3-Gal*p*, 6-Gal*p*, 3,6-Gal*p* residues without any 4,6-Gal*p* linkages is typical for AG-II structures, while 2,4-Gal*p* and 3,4-Gal*p* correspond to AG-I. The Rha residues appeared primarily as 2-Rha*p* and 2,4-Rha*p* along with some T-Rha*p* and 4-Rha*p*. The amount of the 2,4-Rha*p* residue decreased from high to low Mw fractions concurrently with an increase in the abundance of the 2-Rha*p* residue, except in PF5 and PF6. This suggests that compared to high Mw fractions, the backbone of the lower Mw fractions contains less branched Rha residues carrying rather long side chains. Of note, although not changing the conclusion with respect of the structure, the method we used leads to a slight underestimation and overestimation of the Rha and Ara residues, respectively.

PF1 and PF2 displayed a high number of Rha residues that carry branched arabinan and rather short linear galactan (2,4-Rha*p* + 4-Rha*p* ≈ 70 %) side chains. With nearly the same abundance of 3-Gal*p* and 6-Gal*p*, PF1 and PF2 differed only in levels of 3,6-Gal*p* linkage. This indicates that PF1, displaying less 3,6-Gal*p* linkages, is decorated with few but long branches of 6-Gal*p* while PF2 carries slightly more branchpoints but short branches of 6-Gal*p* linked to AG-II backbone.

The proportion of side chains in PF3 is similar to PF2 albeit with a decrease in AG-II components. As compared to PF1 and PF2, the number of branched Rha residues is lower in PF3 and PF4 that contained equal proportions of substituted (2,4-Rha*p* & 4-Rha*p*) and non-substituted (2-Rha*p* & T-Rha*p*) Rha. PF4 was particularly rich in 4-Rha*p*, suggesting the presence of short RG-I backbones having non reducing Rha carrying side chains commonly composed of linear or branched arabinan, or less frequently galactan or AG-I structures, and no typical linkage for AG-II.

PF5 and PF6 were mainly composed of short RG backbones with a low degree of substitution of Rha that are carrying rather long arabinan and less frequently short galactan side chains. Prevalence of T-Rha*p* in PF5 and PF6 suggests that they contain a single Rha attached to a stretch of HG or that Rha is part of an RG-II side chain. These two fractions also exhibit traces of 3-Api*f*, a characteristic sugar for RG-II.

The sum of all the linkages detected in the six PFs is in accordance with the linkages present in cRG-I when considering the proportion of each fraction in the original extract (Table 2). Taken together with the results of monosaccharide composition, the linkage data indicate the presence of over 17 different saccharide linkages in cRG-I. Overall, the linkage analysis confirmed that cRG-I predominantly contains RG structures mainly decorated with arabinan and galactan side chains and some AG-I and AG-II side chains.

3.5. 1D and 2D nuclear magnetic resonance spectroscopy of cRG-I and its fractions

cRG-I and PF1-6 fractions were further characterized using 1D and 2D NMR spectroscopy. The 1D ^{1}H NMR spectra (Fig. 2) showed considerable overlap of signals with different intensities in the anomeric region (5.5–4.0 ppm). The two characteristic high field signals at 1.26 ppm and 1.32 ppm present in all fractions indicate methyl groups of 2-Rha*p* and 2,4-Rha*p*, respectively. The ratio between 2-Rha*p* and 2,4-Rha*p* was calculated based on signal intensity integration (Supplementary Table 2). In accordance with the linkage analysis, the NMR results showed that branched Rha residues (2,4-Rha*p*) were more abundant than unsubstituted Rha (2-Rha*p*) in fraction PF1. The signal intensities between these two residues gradually changed alongside with

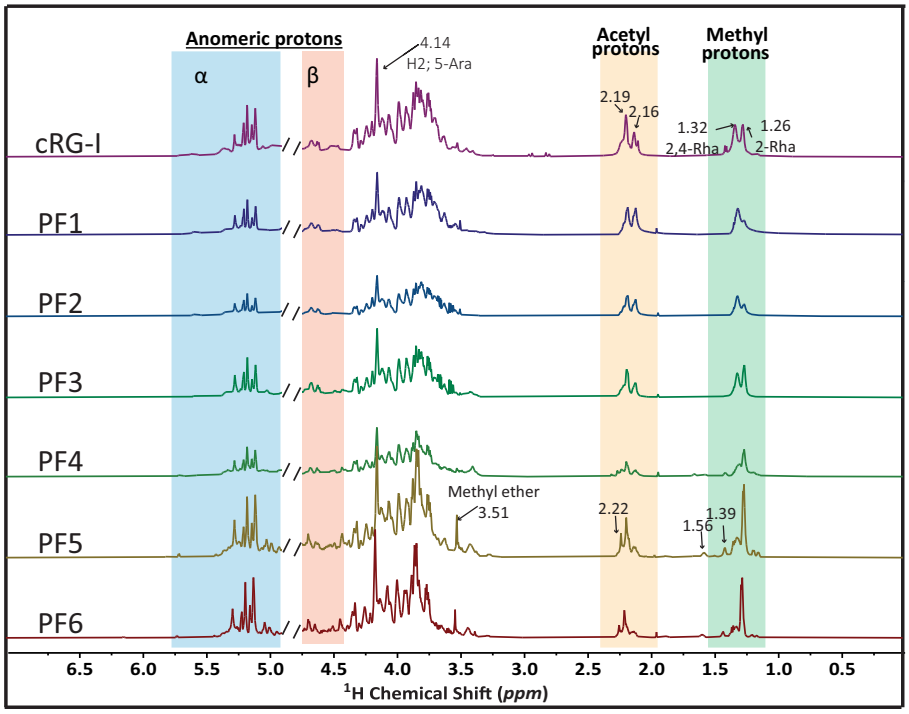

Fig. 2. ^{1}H NMR spectra of cRG-I and its Mw fractions PF1–6. The most distinctive peaks are the diagnostic resonance of 2-Rha*p* and 2,4-Rha*p* (shaded in green), acetyl groups (shaded in yellow), H-1 of β anomers (shaded in orange) and H-1 of α anomers (shaded in blue).

decreasing Mw of the fractions. Of note, 2-Rha*p* was detected in lower quantities in fraction PF6 that contains mainly short oligosaccharides.

Next to methyl group of Rha*p*, all fractions showed the typical signal for *O*-acetyl substitution in the region of δ_H 2.00–2.40. According to previous reports (Perrone et al., 2002; Renard & Jarvis, 1999), signals at δ_H 2.16 and δ_H 2.19 correspond to a single *O*-2/*O*-3 acetyl and a double acetyl substitution on the GalA residues of the RG-I backbone, respectively. In addition, a signal at δ_H 2.22 representing *O*-2/*O*-3 acetyl position on methyl-esterified GalA residues (Renard & Jarvis, 1999) was detected in fractions PF4, PF5 and PF6. Of note, fractions PF5 and PF6 exhibited the characteristic signals for 3,4-Fuc*p* at δ_H 1.56 and for methyl ethers at δ_H 3.51, both diagnostic peaks for RG-II type structures (Barnes et al., 2021), the structure of which was not further analysed in this study.

The 1D ^{1}H NMR spectra (Fig. 2), showed overlapping anomeric signals attributed to α-Ara*f*, α-Rha*p*, α-Gal*p*A (δ_H 4.80–5.80) and β-Gal*p* (δ_H 4.40–4.80), respectively. By means of the 2D ^{1}H—^{13}C HSQC experiment (Fig. 3), the anomeric protons and carbons were assigned (Supplementary Table 3). The comparison of the ^{1}H/^{13}C chemical shifts with previously published data (Sengkhamparn et al., 2009; Westphal et al., 2010) suggested the presence of α-Ara*f* (δ_H/δ_C 5.10–5.25/108.0–112.1), β-Gal*p* (δ_H/δ_C 4.46–4.70/105.6–106.9), α-Rha*p* (δ_H/δ_C 5.16–5.27/99.9–101.4) and α-Gal*p*A (δ_H/δ_C 4.92–5.18/99.4–102.9) residues, respectively.

Our data shows characteristic ^{1}H/^{13}C anomeric signals for nine types of α-Ara*f* residues (A1-A9), five types of β-Gal*p* residues (B1-B5), two to four types of α-Rha*p* residues (C1-C2) and two to three types of α-Gal*p*A (D1-D5) present in all fractions (Sengkhamparn et al., 2009; Westphal et al., 2010). Of note, among all fractions, PF4 had the simplest galactosylation pattern with only two major types of β-Gal*p* anomeric signals at δ_H/δ_C 4.66/106.9 and δ_H/δ_C 4.60/106.9, attributed to T-β-Gal*p* and 4-β-Gal*p*. Ara signals were attributed to T-α-Ara*f*, 5-α-Ara*f*, 3,5-α-Ara*f*, and 2,3,5-α-Ara*f* where there were multiple signals for T-α-Ara*f* resulting from distinct neighbouring group linkages.

2D NMR data shed additional light on 3D conformation of cRG-I populations in solution (Fig. 3). Interestingly, the ^{1}H—^{13}C HSQC NMR spectra of the high Mw PF1 and PF2 fractions showed very weak signals for the backbone sugars (α-Rha*p* & α-GalA*p*) and strong signals for the side chain sugar (α-Ara*f*) despite the fact that the amount of Ara is only slightly higher (≈ 29 mol%) than that of Rha (≈ 20 mol%) and GalA (≈ 21–22 mol%) (Table 1). This may reflect that the long RG-I backbone stretches in PF1 and PF2 are quite rigid in solution while the arabinan side chains are more flexible and this may increase the NMR detection of α-Ara*f* Ara residues. This observation was reported for intact cell wall pectin (Williams et al., 2020) but not yet for RG-I polymers. This discrepancy is less pronounced in the smaller Mw fractions where the RG-I backbone decreases in size while the Ara amount increases (Table 1). The lowest Mw population PF5 and PF6 also showed additional anomeric signals of reducing ends of α-Ara*p*, β-Gal*p*A and β-Glc*p* residues, suggesting the presence of oligomers originating from arabinan, HG and cellulose polymers present in the carrot tissue oligomeric structures. MALDI-TOF-MS analysis of PF6 (Supplementary Fig. 1) confirmed this observation, revealing the masses (*m/z*) corresponding to the [M + Na^{+}] species of arabinan DP 8–30, highly methyl esterified and acetylated HG and short galactan. PF5 and PF6 were the only fractions displaying a signal for α-Fuc*p*.

3.6. *Proposed structures of cRG-I fractions*

Combining the data from monosaccharide composition, apparent Mw and linkage analysis, 2D RG-I structures can be proposed for the PF1–6 fractions (Fig. 4). PF1–3 contain almost pure RG-I (94–98 %; Table 1) and exhibit a similar bottlebrush like structure with long backbones decorated with many rather short side chains. However, PF3 carries less but longer side chains than PF1 and PF2. PF1–3 differ in their Mw, DM% and DA%, which may lead to different conformations as observed by AFM (vide infra). Particularly, the key difference was the presence of methyl esterified HG in PF1 while PF2 showed some methyl esterified RG backbone and almost no HG. PF4 and PF5 correspond to different mixes of shorter RG-I structures and are characterized by somewhat higher HG levels than the other fractions (Table 1). PF5 contains low amounts of typical RG-II sugar residues, while PF6 mainly

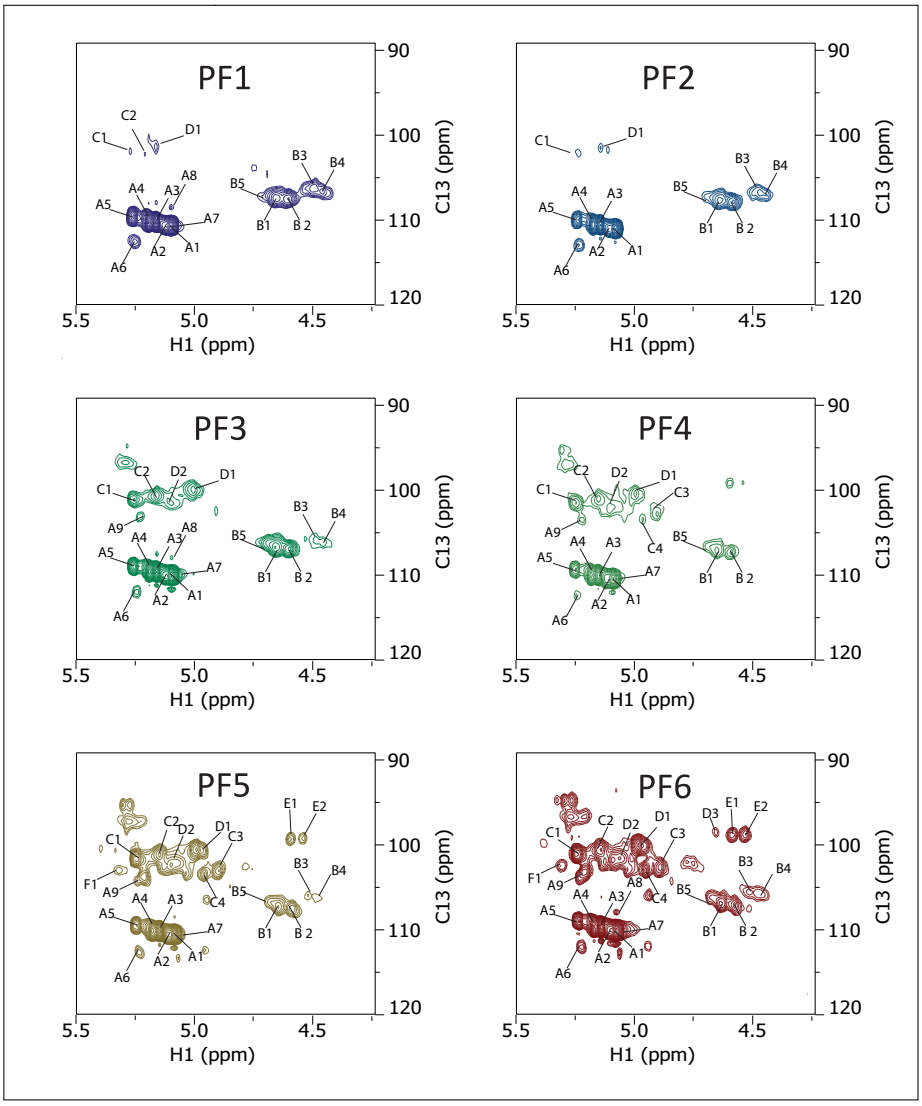

Fig. 3. The anomeric region of 2D ^{1}H-^{13}C HSQC spectra of cRG-I and its fractions (PF1–6). The anomeric signals of different sugar residues are labelled from A to F, where A = α-Ara*f*; B = β-Gal*p*; C = α-Rha*p*; D = α-Gal*p*A; E = β-Glc*p*; F = α-Fuc*p*.

consists of backbone structures (DP 2–6) and long arabinans (DP 8–30), free and/or linked to the backbone and some highly esterified galacturonan (Table 1 and Supplementary Fig. 1).

3.7. Atomic force microscopy imaging

It has been reported that the pectin RG-I regions may adopt different conformations depending on the precise structure, concentration and pH of the solution. This has been visualized by AFM imaging that showed that RG-I may adopt compact structures or expose side chains to the external milieu (Williams et al., 2020; Zdunek et al., 2021). While those studies have mainly been conducted on the RG-I regions of intact pectin from seed mucilage or apple, here we have investigated whether this technique would shed light on the 3D conformation of well-characterized subpopulations of cRG—I.

In AFM height images, the molecules of cRG-I and individual fractions (PF1–6) adopted a similar folded conformation forming spherical aggregates evenly distributed on the mica surface (Fig. 5 and supplementary Fig. 2). The average area occupied by the aggregates was in the range of 200 to 835 nm^2 (Table 3). Aggregates in the original cRG-I extract were the smallest (~ 200 nm^2) and fractionation caused a significant increase in their size. Among fractions, structures in PF1 and PF2 formed very large complexes with an area of about 835 nm^2 and 735 nm^2, respectively. Other fractions (PF3-PF6) had similar moderate sizes of around 500 nm^2. This suggests that sample preparation for AFM imaging facilitated the aggregation of RG-I sub-populations/structures in water. As shown by the elongation parameter, aggregates differed in their shape. The objects in cRG-I had the smallest elongation parameter (0.13) meaning that their shape was closer to regular (circle or square shape has elongation equal 0) while fractionation led to somewhat more elongated aggregates. The fractions PF1 and PF2 both had higher levels of Gal, lower levels of Ara and higher levels of acetylation compared to the other fractions (PF3-PF6). This suggests that combined high levels of side chains containing Gal and Ara had a greater impact on the aggregation capacity of the RG-I structures than high levels of Ara alone. The fractions PF4, PF5 and PF6 displayed quite similar shape characteristics including median height. They are composed of similar structural elements that, however, vary in their relative amounts.

The AFM analysis of cRG-I and its derived fractions showed that after suspension in water all studied samples formed aggregates. The original cRG-I extract showed the most compact spherical/micelle conformation due to interactions between the different structural elements while fractionation led to less compact and elongated aggregates. The backbone length and type of side chains likely impact RG-I aggregation and

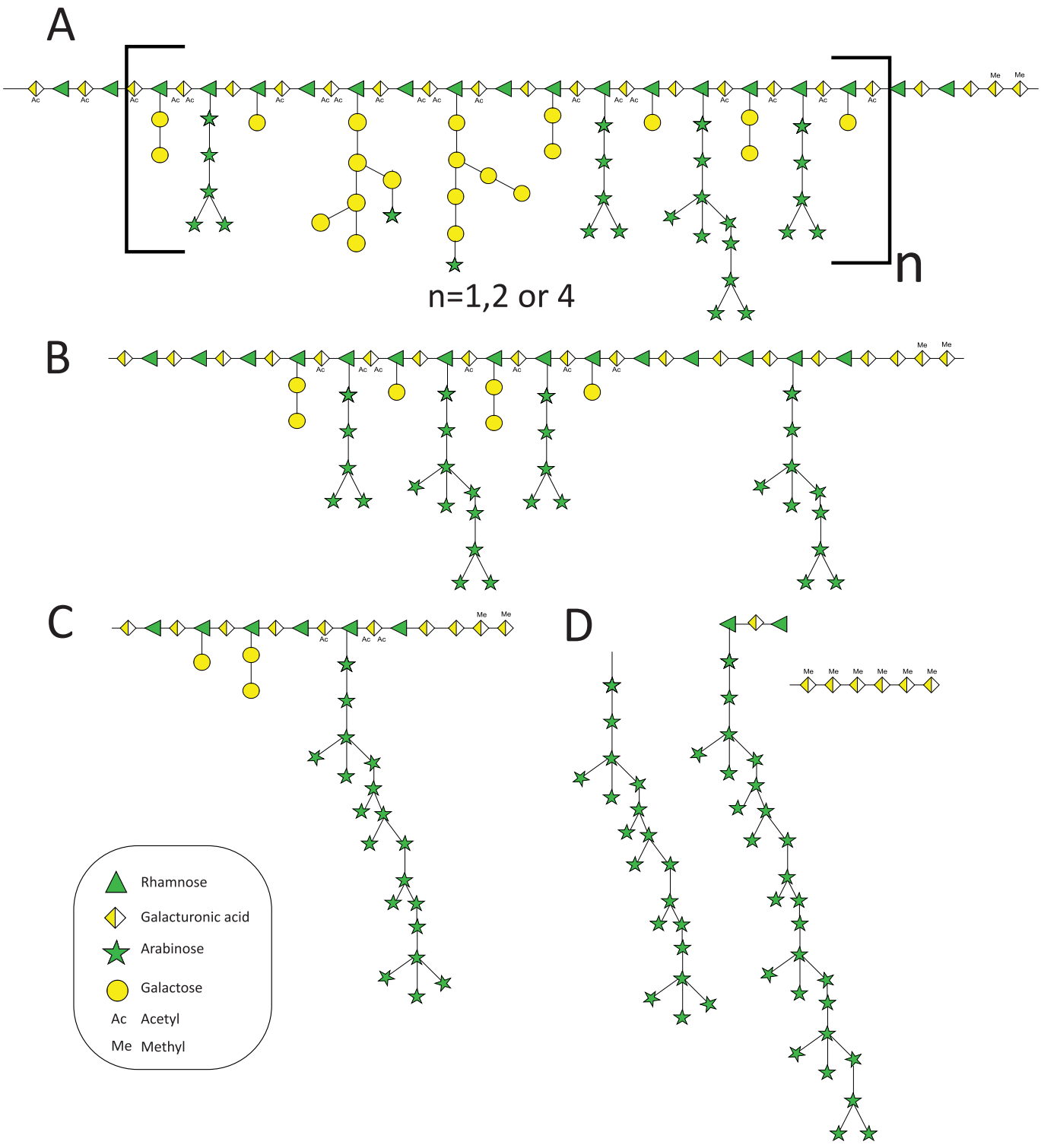

Fig. 4. Proposed chemical 2D structure of RG-I present in cRG-I extract. A) Proposed structure for PF1–3 with $n = 4$, 2 or 1 for PF1, PF2 and PF3, respectively. B) Proposed structure for PF4, C) for PF5 and D) for PF6. The specific sugar symbols are from the symbol nomenclature for glycans (www.ncbi.nlm.nih.gov/glycans/snfg.html).

the shapes observed in AFM. Similar spherical complexes have previously been described for an extract of RG-I isolated from sugar beet pulp, where Rha residues were also highly branched with neutral sugars (Morris et al., 2010; Morris & Ralet, 2012). The backbone length and type of side chains likely impact RG-I aggregation and the shapes observed in AFM. However, without further analyses (e.g. detailed AFM analyses of enzymatically tailored RG-I populations) that are beyond the work presented in this paper, it is difficult to clarify if intra- and/or intermolecular interactions occur via side chains and/or backbones.

3.8. *Immunomodulating properties of cRG-I and derived fractions*

The first papers describing the immune modulatory effect of RG-I extracts from different sources were mostly conducted by studying the

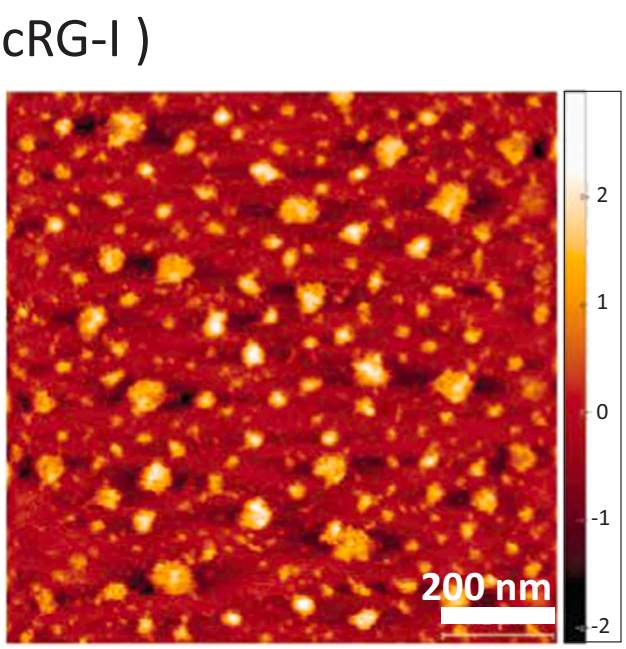

Fig. 5. AFM height image of cRG-I (image size 1 × 1 μm). The scale on the right side of panels represents the height of the observed structure where the black to white color scale translates to −2 to 2 nm of height.

Table 3
Area, elongation and median height of the objects detected on AFM images in cRG-I and fractions PF1–6. Samples with the same letter are not significantly different. Groups were calculated according to HSD Tukey test of the probability of mean differences with alpha level 0.05. Elongation = length of object, area is calculated from the shapes contour (periphery), i.e. the closed polygon that surrounds the feature, and median height = the median of all points inside the object.

Sample	Area nm^2	Elongation	Median Height nm
cRG-I	$200.5^{d} \pm 10.1$	$0.1^{c} \pm 0.0$	$0.1^{b} \pm 0.0$
PF1	$834.8^{c} \pm 14.3$	$0.3^{a} \pm 0.0$	$0.4^{c} \pm 0.0$
PF2	$734.2^{bc} \pm 44.1$	$0.3^{a} \pm 0.0$	$0.3^{a} \pm 0.0$
PF3	$509.7^{a} \pm 13.1$	$0.3^{b} \pm 0.0$	$0.4^{a} \pm 0.0$
PF4	$560.8^{a} \pm 11.4$	$0.3^{a} \pm 0.0$	$0.6^{e} \pm 0.0$
PF5	$543.9^{a} \pm 9.1$	$0.3^{b} \pm 0.0$	$0.6^{d} \pm 0.0$
PF6	$517.6^{a} \pm 13.3$	$0.2^{d} \pm 0.0$	$0.6^{f} \pm 0.0$

cytokine release from macrophages stimulated by said extracts in vitro (Jin et al., 2020; Niu et al., 2023). These studies used pectin extracted by different methods, commonly enriched for HG and containing various amounts of RG-I, with partial or limited structural information. A few follow up studies aimed at linking structural elements of RG-I enriched extracts to their in vitro immunomodulatory effects and these pointed to the importance of the apparent Mw (Nascimento et al., 2017), degree of esterification (Vogt et al., 2016) and role of side chains in the immune effects (Manjegowda et al., 2017; Meijerink et al., 2018; Wu et al., 2020). To the best of our knowledge, more detailed structure function analysis has not been performed with highly enriched extracts such as cRG-I for which we generated detailed structural data by in depth analysis of size separated subpopulations (PF fractions). To assess how specific structural elements influence the cytokine production profile, we used a standardized PBMC assay and measured the secretion of five cytokines (TNF-α, IL-10, IL-6, IL-1β and IL-8) upon stimulation by the fractions. As shown in Fig. 6 (left panels, PF1–6) and in Supplementary Fig. 2 (cRG-I), cRG-I and its fractions induced dose dependent secretion of all cytokines tested, but levels of secretion were cytokine and RG-I fraction specific. PF1 was the most active fraction while surprisingly fraction PF2 appeared inactive, except for a limited induction of IL-8. Fractions PF3–5 were slightly less active than PF6, all notably less potent than PF1. In terms of immunomodulatory profile, cRG-I and PFs stimulated typical pro-inflammatory cytokines (TNF-α, IL-1β and IL-8), a cytokine supporting IgA production (IL-6) and the anti-inflammatory cytokine IL-10, sharing a similar immunomodulation pattern, which seems more complex than a mere pro- or anti-inflammatory effect.

To assess the influence of (non-)esterified residues on the immune response, cRG-I and the PF1–6 fractions were saponified (hereunder designated as PF1-S to PF6-S) leading to the removal of >90 % of the esters. The immune activity of cRG-I was only slightly reduced by alkali treatment (Supplementary Fig. 2). On the contrary, removal of the ester residues (Fig. 6, right panels) led to contrasted effects on PF1 and PF2. PF1-S became largely inactive and induced solely low levels of IL-8 while PF2-S now stimulated the secretion of all cytokines. Fraction PF3-S was twice more active than untreated PF3, which reflects the fact that PF3 contains some subpopulations of PF2 (see Fig. 1B) the activity of which was increased after saponification (PF2-S) (Fig. 6). The fractions PF4, PF5 and PF6 were only marginally affected by saponification.

Notably, cRG-I untreated or saponified (Supplementary Table 4) was less active than some of the fractions, which reflects the fact that it is constituted of a non-proportional mix of six fractions that themselves exhibited low or high potency.

In summary, cRG-I and fractions differing in size and structural elements such as side chains and linkages were examined for their immunomodulating properties, comparing untreated and saponified compounds as an initial step to clarify the structure function relationship of cRG-I. Our data highlight that the high Mw fractions (PF1, PF2 and PF3) are the most active and that their immunomodulating potency is strongly influenced by the degree of esterification, as PF1 is more active than PF1-S while the opposite is observed for PF2 that shows high activity only after removal of the ester residues. This is in line with the reported literature on citrus HG (Jermendi et al., 2023) or less purified pectic extracts (Ferreira et al., 2023) where level and distribution of methyl esters play a role in the immunomodulation capacity showing that lower DM led to higher TLR2/1 dependent immune response of the HG polymer (Jermendi et al., 2023). However, the studies (Ferreira et al., 2015; Wang et al., 2005) on the role of acetyl groups in RG-I and their influence on immunomodulation are scarce. To the best of our knowledge, this is the first study demonstrating the structure dependant effect of acetyl groups on immunomodulation by a purified RG-I extract. The high and low Mw fractions differed in their level of acetyl groups and methyl esters, with DA being higher in PF1–3 than in PF4–6 and DM showing the opposite distribution of those substituents. The lower Mw fractions were less active. PF6 that exhibits a rather different monosaccharide composition, was the most potent of the low Mw fractions. Glycosidic linkage composition and NMR analyses revealed that PF1–3 are characterized by long RG backbones where several Rha residues carry short arabinan, galactan and AG type I and II side chains in contrast especially with PF5 and PF6 that are constituted of shorter backbones where a few Rha residues carry long arabinan or very short galactan side chains (see, Fig. 4). The isolated arabinan, galactan and AG type I and II side chains from various medicinal plants and common crops were described in the literature to be the key effectors for immune modulation (Ferreira et al., 2015; Jin et al., 2020; Niu et al., 2023). Meijerink et al. have shown that the linear and branched arabinans from sugar beet pectin display an immunostimulatory effect in mouse bone marrow derived dendritic cells, especially in their particulate form (Meijerink et al., 2018). We hypothesize that the arabinan and to some extent galactan side chains of cRG-I play an equivalent role in stimulating cytokine production of human PBMCs. Overall, different studies established that all the side chains of RG-I may impact on the immune modulation capacity of RG-I containing extracts.

Taken together, our results suggest that it is not a single element but rather a combination of conformational and structural epitopes, depending on individual sugar residues, specific methyl esters and acetyl

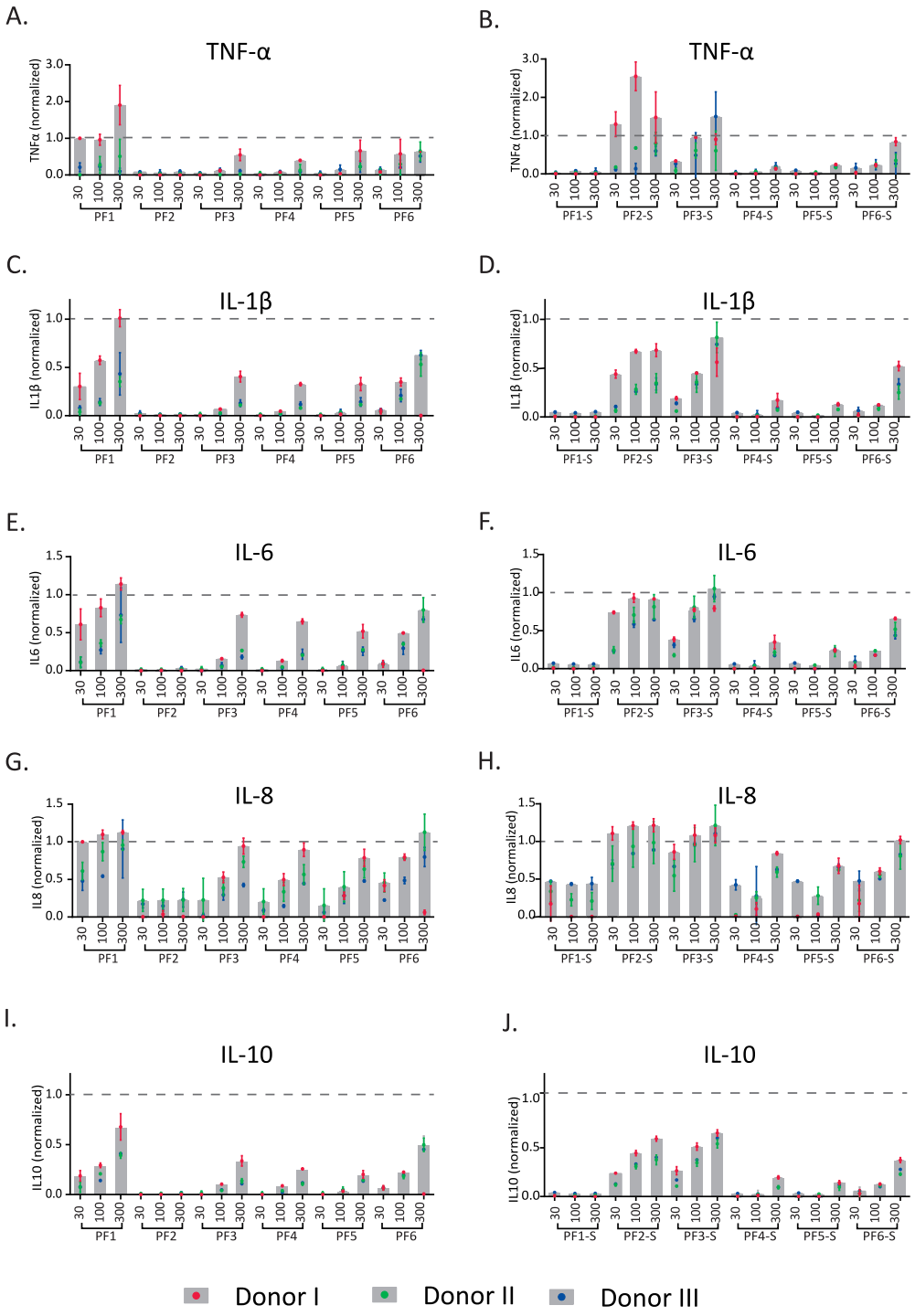

Fig. 6. Cytokine production by PBMCs from three donors stimulated with cRG-I fractions before (left; panel A, C, E, G, I) and after saponification (right: panel B, D, F, H, J). Data were normalized to the LPS response of each donor and for individual cytokines, with LPS (positive control) values fixed to 1. Data represent the mean of three blood donors with each dot corresponding to the mean of technical duplicates.

groups, and charge patterns that play a role in recognition by immune cells. Of note, there was no indication that different DM and DA% modified the pro- or anti-inflammatory profile of the fraction in the PBMC assay.

4. Conclusion

Pectin derived polysaccharides such as RG-I and RG-II are notably complex and polydisperse, which renders the detailed analysis of their structure challenging. Sugar composition and linkage analyses combined with 1D and 2D NMR, and MALDI-TOF-MS led us to propose 2D structures (Fig. 4) of six size-separated fractions of cRG-I. Beyond sugar composition and degree of esterification, the PF1–6 fractions differed strikingly in the nature and the number of sidechains linked to the backbone Rha residues. However, despite composition and structure differences between the fractions, all of them induced the production of the same cytokines in an in vitro immune assay, but differed in (relative) amounts of cytokines produced and consequently in their biological potency with the large Mw fractions being most active. The degree of esterification of the fractions played a definitive role in their immune

profile, with the still unexplained observation that PF1 was more active when intact while PF2 displayed activity only after saponification having all methyl and acetyl esters removed. The first AFM studies showed that a less compact structure was in line with higher immune stimulation capacity. However, in depth AFM analyses will be required with compounds resuspended in conditions similar to those of the in vitro assays, or even mimicking the gut lumen milieu. We currently hypothesize that, beyond the presence and repartition of ester residues, the 2D and 3D conformations of cRG-I derived fractions play a critical role in their immune signalling as a result of a differential exposure of structural and conformational epitopes. This should be further investigated by enzymatically and or chemically modifying side chains and esters and measuring how this affects the immune potency of the tailored compounds.

CRediT authorship contribution statement

Krishna Desai: Writing – review & editing, Writing – original draft, Visualization, Validation, Software, Methodology, Investigation, Formal analysis, Data curation, Conceptualization. **Justyna Dobruchowska:** Methodology, Investigation, Writing – review & editing. **Kari Elbers:** Methodology. **Justyna Cybulska:** Methodology, Investigation, Data curation. **Artur Zdunek:** Writing – review & editing, Validation, Investigation, Data curation. **Mojtaba Porbahaie:** Methodology, Investigation. **Erik Jansen:** Methodology. **Joost Van Neerven:** Writing – review & editing, Investigation, Data curation. **Ruud Albers:** Writing – review & editing, Funding acquisition. **Tom Wennekes:** Writing – review & editing, Supervision, Funding acquisition. **Annick Mercenier:** Writing – review & editing, Validation, Supervision, Funding acquisition, Conceptualization. **Henk A. Schols:** Writing – review & editing, Validation, Supervision, Conceptualization.

Declaration of competing interest

The authors declare the following financial interests which may be considered as potential competing interests. NutriLeads holds intellectual property rights for the use cRG-I. Annick Mercenier and Ruud Albers were employed at NutriLeads and remain shareholders affiliated to NutriLeads for scientific matters.

Data availability

Data will be made available on request.

Acknowledgements

The authors would like to thank Peter de Gijssel for technical GC support, Edwin Bakx for helping with PMAAs data analysis and Margaret Bosveld for an introduction to preparative SEC.

Funding sources

This research has received funding from the European Union's Horizon 2020 research and innovation programme as part of funding Programme Marie Skłodowska-Curie ITN 2018 under grant agreement No 814102.

Appendix A. Supplementary data

Supplementary data to this article can be found online at https://doi.org/10.1016/j.carbpol.2024.122730.

References

Barnes, W. J., Koj, S., Black, I. M., Archer-Hartmann, S. A., Azadi, P., Urbanowicz, B. R., … O'Neill, M. A. (2021). Protocols for isolating and characterizing polysaccharides from plant cell walls: A case study using rhamnogalacturonan-II. *Biotechnology for Biofuels, 14*, 142. https://doi.org/10.1186/s13068-021-01992-0

Beukema, M., Faas, M. M., & de Vos, P. (2020). The effects of different dietary fiber pectin structures on the gastrointestinal immune barrier: Impact via gut microbiota and direct effects on immune cells. *Experimental and Molecular Medicine, 52*, 1364–1376. https://doi.org/10.1038/s12276-020-0449-2

Black, I., Heiss, C., Carlson, R. W., & Azadi, P. (2021). Linkage analysis of oligosaccharides and polysaccharides: A tutorial. In A. Delobel (Ed.), *Vol. 2271. Mass spectrometry of glycoproteins: Methods and protocols* (pp. 249–271). Springer US. https://doi.org/10.1007/978-1-0716-1241-5_18.

Blumenkrantz, N., & Asboe-Hansen, G. (1973). New method for quantitative determination of uronic acids. *Analytical Biochemistry, 54*, 484–489. https://doi.org/10.1016/0003-2697(73)90377-1

Brouns, F., Theuwissen, E., Adam, A., Bell, M., Berger, A., & Mensink, R. P. (2012). Cholesterol-lowering properties of different pectin types in mildly hypercholesterolemic men and women. *European Journal of Clinical Nutrition, 66*, 591–599. https://doi.org/10.1038/ejcn.2011.208

Caffall, K. H., & Mohnen, D. (2009). The structure, function, and biosynthesis of plant cell wall pectic polysaccharides. *Carbohydrate Research, 344*, 1879–1900. https://doi.org/10.1016/j.carres.2009.05.021

Cybulska, J., Halaj, M., Cepák, V., Lukavský, J., & Capek, P. (2016). Nanostructure features of microalgae biopolymer. *Starch - Stärke, 68*, 629–636. https://doi.org/10.1002/star.201500159

De Ruiter, G. A., Schols, H. A., Voragen, A. G. J., & Rombouts, F. M. (1992). Carbohydrate analysis of water-soluble uronic acid-containing polysaccharides with high-performance anion-exchange chromatography using methanolysis combined with TFA hydrolysis is superior to four other methods. *Analytical Biochemistry, 207*, 176–185. https://doi.org/10.1016/0003-2697(92)90520-H

Desai, K., Van den Abbeele, P., Duysburgh, C., Albers, R., Wennekes, T., Schols, H. A., & Mercenier, A. (2024). Structure dependent fermentation kinetics of dietary carrot rhamnogalacturonan-I in an in vitro gut model. *Food Hydrocolloids, 153, Article 110036*. https://doi.org/10.1016/j.foodhyd.2024.110036

Donadio, J. L. S., & Fabi, J. P. (2024). Comparative analysis of pectin and prebiotics on human microbiota modulation in early life stages and adults. *Food & Function, 15*, 6825–6846. https://doi.org/10.1039/d4fo01231c

Dranca, F., & Oroian, M. (2018). Extraction, purification and characterization of pectin from alternative sources with potential technological applications. *Food Research International, 113*, 327–350. https://doi.org/10.1016/j.foodres.2018.06.065

Ferreira, S. S., Correia, A., Silva, A. M. S., Wessel, D. F., Cardoso, S. M., Vilanova, M., & Coimbra, M. A. (2023). Structure-function relationships of pectic polysaccharides from broccoli by-products with in vitro B lymphocyte stimulatory activity. *Carbohydrate Polymers, 303, Article 120432*. https://doi.org/10.1016/j.carbpol.2022.120432

Ferreira, S. S., Passos, C. P., Madureira, P., Vilanova, M., & Coimbra, M. A. (2015). Structure–function relationships of immunostimulatory polysaccharides: A review. *Carbohydrate Polymers, 132*, 378–396. https://doi.org/10.1016/j.carbpol.2015.05.079

Ho, G. T. T., Zou, Y. F., Wangensteen, H., & Barsett, H. (2016). RG-I regions from elderflower pectins substituted on GalA are strong immunomodulators. *International Journal of Biological Macromolecules, 92*, 731–738. https://doi.org/10.1016/j.ijbiomac.2016.07.090

Huang, C.-N., Wang, C.-J., Lee, Y.-J., & Peng, C.-H. (2017). Active subfractions of Abelmoschus esculentus substantially prevent free fatty acid-induced β cell apoptosis via inhibiting dipeptidyl peptidase-4. *PLoS One, 12*(7), Article e0180285. https://doi.org/10.1371/journal.pone.0180285

Jermendi, E., Fernandez-Lainez, C., Beukema, M., Lopez-Velazquez, G., van den Berg, M. A., de Vos, P., & Schols, H. A. (2023). TLR 2/1 interaction of pectin depends on its chemical structure and conformation. *Carbohydrate Polymers, 303*, Article 120444. https://doi.org/10.1016/j.carbpol.2022.120444

Jin, M.-Y., Li, M.-Y., Huang, R.-M., Wu, X.-Y., Sun, Y.-M., & Xu, Z.-L. (2020). Structural features and anti-inflammatory properties of pectic polysaccharides: A review. *Trends in Food Science & Technology, 107*, 284–298. https://doi.org/10.1016/j.tifs.2020.10.042

Kiyohara, H., Matsumoto, T., & Yamada, H. (2002). Intestinal immune system modulating polysaccharides in a Japanese herbal (Kampo) medicine. *Juzen-Taiho-To. Phytomedicine, 9*(7), 614–624. https://doi.org/10.1078/094471102321616427

Kwak, B.-S., Hwang, D., Lee, S. J., Choi, H.-J., Park, H.-Y., & Shin, K.-S. (2019). Rhamnogalacturonan-I-type polysaccharide purified from broccoli exerts antimetastatic activities via innate immune cell activation. *Journal of Medicinal Food, 22*(5), 451–459. https://doi.org/10.1089/jmf.2018.4286

Lee, H. B., Son, S. U., Lee, J. E., Lee, S. H., Kang, C. H., Kim, Y. S., … Park, H. Y. (2021). Characterization, prebiotic and immune-enhancing activities of rhamnogalacturonan-I-rich polysaccharide fraction from molokhia leaves. *International Journal of Biological Macromolecules, 175*, 443–450. https://doi.org/10.1016/j.ijbiomac.2021.02.019

Lutter, R., Teitsma-Jansen, A., Floris, E., Lone-Latif, S., Ravi, A., Pineros, Y. S. S., … Albers, R. (2021). The dietary intake of carrot-derived Rhamnogalacturonan-I accelerates and augments the innate immune and anti-viral interferon response to rhinovirus infection and reduces duration and severity of symptoms in humans in a randomized trial. *Nutrients, 13*(12), 4395. https://doi.org/10.3390/nu13124395

Manjegowda, S. B., Rajagopal, H. M., & Dharmesh, S. M. (2017). Polysaccharide of Black cumin (Nigella sativa) modulates molecular signaling cascade of gastric ulcer pathogenesis. *International Journal of Biological Macromolecules, 101*, 823–836. https://doi.org/10.1016/j.ijbiomac.2017.03.093

McKay, S., Oranje, P., Helin, J., Koek, J. H., Kreijveld, E., van den Abbeele, P., … Albers, R. (2021). Development of an affordable, sustainable and efficacious plant-

based immunomodulatory food ingredient based on Bell pepper or carrot RG-I Pectic polysaccharides. *Nutrients, 13*(3), 963. https://doi.org/10.3390/nu13030963
McKay, S., Teitsma-Jansen, A., Floris, E., Dekker, T., Smids, B., Khurshid, R., … Albers, R. (2022). Effects of dietary supplementation with carrot-derived Rhamnogalacturonan-I (cRG-I) on accelerated protective immune responses and quality of life in healthy volunteers challenged with rhinovirus in a randomized trial. *Nutrients, 14*(20), 4258. https://doi.org/10.3390/nu14204258
Meijerink, M., Rösch, C., Taverne, N., Venema, K., Gruppen, H., Schols, H. A., & Wells, J. M. (2018). Structure dependent-immunomodulation by sugar beet Arabinans via a SYK tyrosine kinase-dependent signaling pathway. *Frontiers in Immunology, 9*, 1972. https://doi.org/10.3389/fimmu.2018.01972
Morris, G. A., & Ralet, M.-C. (2012). The effect of neutral sugar distribution on the dilute solution conformation of sugar beet pectin. *Carbohydrate Polymers, 88*(4), 1488–1491. https://doi.org/10.1016/j.carbpol.2012.02.020
Morris, G. A., Ralet, M.-C., Bonnin, E., Thibault, J.-F., & Harding, S. E. (2010). Physical characterisation of the rhamnogalacturonan and homogalacturonan fractions of sugar beet (Beta vulgaris) pectin. *Carbohydrate Polymers, 82*(4), 1161–1167. https://doi.org/10.1016/j.carbpol.2010.06.049
Nascimento, G. E.d., Iacomini, M., & Cordeiro, L. M. C. (2017). New findings on green sweet pepper (Capsicum annum) pectins: Rhamnogalacturonan and type I and II arabinogalactans. *Carbohydrate Polymers, 171*, 292–299. https://doi.org/10.1016/j.carbpol.2017.05.029
Ndeh, D., Rogowski, A., Cartmell, A., Luis, A. S., Basle, A., Gray, J., … Gilbert, H. J. (2017). Complex pectin metabolism by gut bacteria reveals novel catalytic functions. *Nature, 544*(7648), 65–70. https://doi.org/10.1038/nature21725
Niu, H., Dou, Z. M., Hou, K. K., Wang, W. D., Chen, X. X., Chen, X. W., … Fu, X. (2023). A critical review of RG-I pectin: Sources, extraction methods, structure, and applications. *Critical Reviews in Food Science and Nutrition, 1-21*. https://doi.org/10.1080/10408398.2023.2204509
Perrone, P., Hewage, C. M., Thomson, A. R., Bailey, K., Sadler, I. H., & Fry, S. C. (2002). Patterns of methyl and O-acetyl esterification in spinach pectins: New complexity. *Phytochemistry, 60*(1), 67–77. https://doi.org/10.1016/S0031-9422(02)00039-0
Porbahaie, M., Ulfman, L. H., Prodan, A., Teodorowicz, M., Schloesser, J. E. L., Savelkoul, H. F. J., … van Neerven, R. J. J. (2024). Dietary intervention with whey protein concentrate does not affect toll-like receptor responses and gene expression patterns in peripheral blood mononuclear cells of healthy volunteers. *Nutrients, 16*(5), 592. https://doi.org/10.3390/nu16050592
Renard, C. M. G. C., & Jarvis, M. C. (1999). Acetylation and methylation of homogalacturonans 2: Effect on ion-binding properties and conformations. *Carbohydrate Polymers, 39*(3), 209–216. https://doi.org/10.1016/S0144-8617(99)00015-6
Reynolds, A., Mann, J., Cummings, J., Winter, N., Mete, E., & Morenga, L. T. (2019). Carbohydrate quality and human health: A series of systematic reviews and meta-analyses. *The Lancet, 393*(10170), 434–445. https://doi.org/10.1016/s0140-6736(18)31809-9
Roman-Benn, A., Contador, C. A., Li, M.-W., Lam, H.-M., Ah-Hen, K., Ulloa, P. E., & Ravanal, M. C. (2023). Pectin: An overview of sources, extraction and applications in food products, biomedical, pharmaceutical and environmental issues. *Food Chemistry Advances, 2*, Article 100192. https://doi.org/10.1016/j.focha.2023.100192
Schwab, U., Louheranta, A., Torronen, A., & Uusitupa, M. (2006). Impact of sugar beet pectin and polydextrose on fasting and postprandial glycemia and fasting concentrations of serum total and lipoprotein lipids in middle-aged subjects with abnormal glucose metabolism. *European Journal of Clinical Nutrition, 60*(9), 1073–1080. https://doi.org/10.1038/sj.ejcn.1602421
Sengkhamparn, N., Bakx, E. J., Verhoef, R., Schols, H. A., Sajjaanantakul, T., & Voragen, A. G. (2009). Okra pectin contains an unusual substitution of its rhamnosyl residues with acetyl and alpha-linked galactosyl groups. *Carbohydrate Research, 344*(14), 1842–1851. https://doi.org/10.1016/j.carres.2008.11.022
Son, S. U., Choi, E. H., & Shin, K. S. (2023). Effects of rhamnogalacturonan-I type polysaccharide purified from Curcuma longa on immunostimulatory and intracellular signaling pathway mechanisms of macrophages. *Food Bioscience, 53*, Article 102589. https://doi.org/10.1016/j.fbio.2023.102589
SPIP Reference guide. (2024). Retrieved 01 February 2024 from https://www.imagemet.com/WebHelp6/Default.htm#PnPParameters/Measure_Shape_Parameters.htm?Highlight=elongation.
Tang, X., & de Vos, P. (2023). Structure-function effects of different pectin chemistries and its impact on the gastrointestinal immune barrier system. *Critical Reviews in Food Science and Nutrition, 1-15*. https://doi.org/10.1080/10408398.2023.2290230
Thibault, J. F. (1979). Automated-method for the determination of pectic substances. *Lebensmittel-Wissenschaft & Technologie, 12*(5), 247–251.
Van den Abbeele, P., Duysburgh, C., Cleenwerck, I., Albers, R., Marzorati, M., & Mercenier, A. (2021). Consistent prebiotic effects of carrot RG-I on the gut microbiota of four human adult donors in the SHIME((R)) model despite baseline individual variability. *Microorganisms, 9, Article 2142*. https://doi.org/10.3390/microorganisms9102142
Van den Abbeele, P., Verstrepen, L., Ghyselinck, J., Albers, R., Marzorati, M., & Mercenier, A. (2020). A novel non-digestible, Carrot-Derived Polysaccharide (cRG-I) selectively modulates the human gut microbiota while promoting gut barrier integrity: An integrated in vitro approach. *Nutrients, 12*, 1917. https://doi.org/10.3390/nu12071917
Vogt, L. M., Sahasrabudhe, N. M., Ramasamy, U., Meyer, D., Pullens, G., Faas, M. M., … d.. (2016). The impact of lemon pectin characteristics on TLR activation and T84 intestinal epithelial cell barrier function. *Journal of Functional Foods, 22*, 398–407. https://doi.org/10.1016/j.jff.2016.02.002
Voragen, A. G. J., Coenen, G.-J., Verhoef, R. P., & Schols, H. A. (2009). Pectin, a versatile polysaccharide present in plant cell walls. *Structural Chemistry, 20*, 263–275. https://doi.org/10.1007/s11224-009-9442-z
Wang, X. S., Liu, L., & Fang, J. N. (2005). Immunological activities and structure of pectin from Centella asiatica. *Carbohydrate Polymers, 60*, 95–101. https://doi.org/10.1016/j.carbpol.2004.11.031
Westphal, Y., Kuhnel, S., de Waard, P., Hinz, S. W., Schols, H. A., Voragen, A. G., & Gruppen, H. (2010). Branched arabino-oligosaccharides isolated from sugar beet arabinan. *Carbohydrate Research, 345*(9), 1180–1189. https://doi.org/10.1016/j.carres.2010.03.042
Williams, M. A. K., Cornuault, V., Irani, A. H., Symonds, V. V., Malmström, J., An, Y., … North, H. M. (2020). Polysaccharide structures in the outer mucilage of Arabidopsis seeds visualized by AFM. *Biomacromolecules, 21*(4), 1450–1459. https://doi.org/10.1021/acs.biomac.9b01756
Wu, D., Zheng, J., Mao, G., Hu, W., Ye, X., Linhardt, R. J., & Chen, S. (2020). Rethinking the impact of RG-I mainly from fruits and vegetables on dietary health. *Critical Reviews in Food Science and Nutrition, 60*(17), 2938–2960. https://doi.org/10.1080/10408398.2019.1672037
Yapo, B. M. (2011). Rhamnogalacturonan-I: A structurally puzzling and functionally versatile polysaccharide from plant cell walls and Mucilages. *Polymer Reviews, 51*(4), 391–413. https://doi.org/10.1080/15583724.2011.615962
Zdunek, A., Pieczywek, P. M., & Cybulska, J. (2021). The primary, secondary, and structures of higher levels of pectin polysaccharides. *Comprehensive Reviews in Food Science and Food Safety, 20*(1), 1101–1117. https://doi.org/10.1111/1541-4337.12689